Structural transformations of the La2–xPrxNiO4+δ system probed by high-resolution synchrotron and neutron powder diffraction

Vaibhav Vibhu, Matthew R. Suchomel, Nicolas Penin, François Weill, Jean-Claude Grenier, Jean-Marc. Bassat, Aline Rougier

Structural transformations of the $La_{2-x}Pr_xNiO_{4+\delta}$ system probed by high-resolution synchrotron and neutron powder diffraction

Vaibhav Vibhu [a,b], Matthew R. Suchomel †[a,b], Nicolas Penin [a,b], François Weill [a,b], Jean-Claude Grenier [a,b], Jean-Marc Bassat [a,b], and Aline Rougier [a,b]

Compositions in the $La_{2-x}Pr_xNiO_{4+\delta}$ series offer an attractive balance of chemical stability and electrochemical performance for use as cathode materials in solid oxide fuel cells (SOFCs). A detailed crystallographic study of this system has been performed, combining both high resolution synchrotron and neutron powder diffraction data, in order to investigate structural details of the series as a function of composition, temperature and oxygen over-stoichiometry. The monoclinic structure (space group *F*2/*m*) of ambient temperature Pr-rich compositions for $1.0 < x \leq 2.0$ is discussed in terms of octahedra tilt arrangements and possible long-range structural modulations. *In situ* synchrotron diffraction experiments and TEM are employed to examine the role of temperature and interstitial oxygen on these structural distortions. With increasing La substitution, a region of mixed monoclinic and tetragonal phases is described for $0.5 \leq x \leq 1.0$. La-rich compositions are found to be single phase tetragonal (*F*4/*mmm* for $0 < x < 0.5$) or orthorhombic (*Fmmm* for $x = 0$). Possible origins and electrochemical property consequences of the refined structural trends are considered.

1. Introduction

Transition metal oxides exhibiting mixed ionic and electronic conductivity (MIEC) are attractive candidates for cathode materials in solid oxide fuel cells (SOFCs) and oxygen separation membranes.[1-3] While SOFCs afford direct and highly efficient conversion of chemical to electrical energy, the high typical operating temperatures (800-1000 °C) increase device assembly costs and reduce chemical stability of cell components. Consequently, there is considerable interest in improving intermediate temperature (IT-SOFCs) devices operating in a lower temperature range of 600 – 700 °C.[4] However, as both electrode reaction kinetics and electrolyte ion transport mechanisms are temperature dependent, electrochemical performance typically suffers as the temperature is reduced. Problems of high cathode polarization resistance (R_p), induced by slow oxygen reduction processes, are a particular challenge in developing improved IT-SOFCs. By combining adequate coefficients of oxygen exchange and diffusion with reasonable electronic conductivities, MIEC oxide materials based on perovskite or related derivative structures afford some of best reported performance for IT-SOFC cathode applications.[5] This includes the layered Ruddlesden–Popper (RP) type Ln_2MO_4 structures in which oxygen ions can be transported interstitialcy along rock-salt layers separated by slabs of transition metal ions situated in octahedral sites (typical MIEC compositions have *Ln* = La, Nd, Pr; and *M* = Cu, Ni, Co).[6,7]

In particular, the RP-type rare earth nickelates $Ln_2NiO_{4+\delta}$ have been shown to exhibit good cathodic performance.[8] The general structure for this first member of the RP series consists of alternate NiO_2 square plane layers and Ln_2O_2 rock salt type-layers. This type of structure readily accepts interstitial oxygen ions in the Ln_2O_2 rock-salt interlayer, leading to a mixed $Ni^{2+/3+}$ valence, and thus mixed ionic and electronic conductivity (O^{2-}/e^-).[8] The interstitial oxygen value δ is strongly dependent on the size of *Ln* cation radii and can be influenced by annealing conditions.

Regarding previous research on $Ln_2NiO_{4+\delta}$ (*Ln* = La, Nd or Pr) compounds, $Pr_2NiO_{4+\delta}$ (PNO) showed the lowest polarization resistance when measured with a Gd-doped ceria (GDC) interface and a yttria-substituted zirconia (YSZ) electrolyte.[9] Despite these promising electrochemical properties at intermediate temperatures, PNO has rather poor thermodynamic stability in comparison to $La_2NiO_{4+\delta}$ (LNO). Under oxidizing atmospheres at elevated temperatures, it has been shown that $Pr_2NiO_{4+\delta}$ can decompose to a mixture of $Pr_4Ni_3O_{10}$, $PrNiO_{3-\delta}$, and PrO_x.[10-14] For this reason, there has been recent interest in mixed PNO-LNO compositions which could offer a compromise of chemical stability and electrochemical performance.[15-19] However, despite investigations spanning three decades, the phase diagram of the $La_{2-x}Pr_xNiO_{4+\delta}$ system; as a function of composition, oxygen stoichiometry, and temperature, is still unclear. In the current work, a fundamental crystallographic study of the $La_{2-x}Pr_xNiO_{4+\delta}$ series has been performed using high resolution synchrotron and neutron powder diffraction data. This work aims to provide context of previous work on $La_{2-x}Pr_xNiO_{4+\delta}$, and to help further clarify structural details of this series (as a function of composition, temperature and oxygen over-stoichiometry) in order to promote the identification of optimized MIEC compositions.

2. Background

Both of the parent compounds $La_2NiO_{4+\delta}$ and $Pr_2NiO_{4+\delta}$ were examined by Goodenough *et al*. more than 30 years ago with other Cu^{2+} and Ni^{2+} containing K_2NiF_4-type oxides.[20] At high temperature these compounds adopt a tetragonal structure. On cooling, the strain of increasingly mismatched bond distances between the *Ln*-O and Ni-O layers can be reduced by tilting of NiO_6 octahedra, which results in several structural phase transitions to lower symmetries. This layer mismatch strain is also partially offset by the insertion of interstitial oxygen ions in the Ln_2O_2 layer.[21]

The discovery of superconductivity in related La_2CuO_4-type oxides motivated further studies of these compounds in the early 1990's.[22] Jorgensen *et al*. and Rodriguez-Carvajal *et al*. used neutron powder diffraction (NPD) to study $La_2NiO_{4+\delta}$ as a function of temperature for different metal oxidation state values.[23,24] A tetragonal *I*4/*mmm* structure was found at high temperatures,

but ambient and low temperature structures of $La_2NiO_{4+\delta}$ were found to vary with oxygen content. The stoichiometric ($\delta \approx 0.0$) composition showed a single *Bmab* orthorhombic phase at ambient temperature, while oxygen-rich compositions ($\delta > 0.14$) exhibited an *F*4/*mmm* orthorhombic structure incorporating an interstitial oxygen ion located near the (¼, ¼, ¼) position in the unit cell. Intermediate oxygen values ($0.02 < \delta < 0.14$) were described by mixed phase coexistence regions of *Bmab*, $P4_2/ncm$, *Pccn*, or *F*4/*mmm* structures. Subsequent X-ray diffraction and thermogravimetry studies by Buttrey *et al*. and Tamura *et al.* broadly supported these findings while adding greater details to the proposed $La_2NiO_{4+\delta}$ phase diagram.[25-28] Demourgues *et al.* showed how an electrochemical process could increase interstitial oxygen content in $La_2NiO_{4+\delta}$ up to $\delta \approx 0.25$, and used TEM to determine an expanded *C*2 monoclinic unit cell accommodating additional oxygen ordering.[29,30] More recent structural studies of non-stoichiometric $La_2NiO_{4+\delta}$ compositions have focused on low temperature orthorhombic (LTO) and high temperature tetragonal (HTT) structures under variable oxygen partial pressures, reflecting a shift of research focus on these materials from superconductivity towards the mixed ionic-electronic conductivity properties of layered rare earth nickelates.[31-33]

Despite early initial conjecture of a monoclinic structural distortion for $Pr_2NiO_{4+\delta}$,[20,34,35] most subsequent studies reported orthorhombic or tetragonal structures depending on temperature and oxygen δ content.[10,36-41] Sullivan *et al.* examined a wide range of non-stoichiometric $Pr_2NiO_{4+\delta}$ oxygen values ($0 \leq \delta < 0.22$) and proposed a phase diagram with multiple single and mixed-phase regions distinguished by different canting arrangements of NiO_6 octahedra. For higher excess oxygen values ($\delta > 0.17$) they observed additional weak diffraction peaks which could not be explained nor indexed by the proposed *Fmmm* orthorhombic structures.[10] $Pr_2NiO_{4+\delta}$ was also extensively probed by Fernández-Díaz *et al*. who found magnetic ordering in a tetragonal structure at low temperatures (< 120 K) for near oxygen stoichiometric compositions ($\delta < 0.02$); samples with higher oxygen excess values ($\delta \approx 0.20$) displayed an "*average*" orthorhombic structure at ambient temperature (with similar weak superlattice type NPD peaks not indexed by the assigned *Bmab* cell) which transformed to a tetragonal cell above 690 K.[38,39] Similarly, Allançon *et al*. described a low temperature tetragonal (LTT) $P4_2/ncm$ region in $Pr_2NiO_{4+\delta}$ for low δ values; whereas more oxidized compositions with $0.09 < \delta < 0.22$ maintained a LTO *Bmab* structure with weak unindexed supercell peaks until a HTT phase transition to $P4_2/ncm$ near 700 K. The precise HTT transition temperature varied slightly with initial oxygen δ value.[40,41] Under low pO_2 conditions ($\approx 10^{-4}$ atm) Flura *et al.* report a transition in $Pr_2NiO_{4+\delta}$ at approximately 675 K from a LTO over-stoichiometric to a different high temperature orthorhombic structure.[33] Later studies have focused primarily on the stability, oxygen diffusion mechanisms and electrochemical properties of $Pr_2NiO_{4+\delta}$.[9,11,42-45]

Recently, Hernandez *et al*. used high angular resolution synchrotron powder diffraction to establish that, in fact, oxidized $Pr_2NiO_{4+\delta}$ compositions ($\delta \approx 0.22$) do exhibit a clear but subtle monoclinic distortion at ambient temperature.[46] This so-called low temperature monoclinic cell (LTM) was indexed with a *F*2/*m* space group (non-conventional setting of space group nº 12, *C*2/*m*), and is derived from the parent orthorhombic *Fmmm* cell, but with one non-90° angle of $\gamma \approx 90.06°$. *In situ* studies showed that the monoclinic distortion persists until the transition to a HTT form above 700 K. As mentioned above for previous $Pr_2NiO_{4+\delta}$ works, Hernandez *et al.* also observe weak non-indexed reflections in diffraction patterns, which they attribute to complex incommensurate modulation, for which the average structure can be described by the proposed LTM cell. Nevertheless, perhaps due to microstructural effects and/or insufficient diffraction data resolution, succeeding reports continue to use orthorhombic structures for $Pr_2NiO_{4+\delta}$.[19,47]

Despite this extensive literature on both LNO and PNO end members, relatively few bulk ceramic structural studies have considered the full $La_{2-x}Pr_xNiO_{4+\delta}$ (LPNO) system. While some studies did not consider any structural details,[15] both Allançon *et al.* and Miyake *et al.* claimed single phase orthorhombic structures across the LPNO system,[16,48] indexing Pr-rich ($x > 1.0$) and La-rich cell ($x < 1.0$) compositions with *Bmab* and *Fmmm* space groups, respectively. Vibhu *et al*. used similar structural indexing, but noted the presence of mixed phase region (*Bmab* and *Fmmm*) for La rich LPNO compositions with $0.5 < x < 1.0$.[17]

In this current work, compositions of the series $La_{2-x}Pr_xNiO_{4+\delta}$ are re-examined in light of both the average monoclinic structural distortion for PNO now clearly established by Hernandez *et al*., and the recent interest in optimized chemical stability and MIEC properties for mixed LNO-PNO phases. High-resolution data from synchrotron, neutron and TEM probes are used to study the ambient temperature structural characteristics for selected oxidized LPNO compositions. Details of the monoclinic distortion and weak supercell reflections for Pr-rich compositions, as well as the mixed phase region for La-rich samples, are then discussed in the context of understanding the crystallography of $La_{2-x}Pr_xNiO_{4+\delta}$ and informing future research on this promising SOFC cathode material.

3. Experimental

3.1 Synthesis

$La_{2-x}Pr_xNiO_{4+\delta}$ compositions for the range $0.0 \leq x \leq 2.0$ were prepared *via* a citrate-nitrate route from Pr_6O_{11} (Aldrich, 99.9%), La_2O_3 (Strem Chemical, 99.99%) and $Ni(NO_3)_2{\cdot}6H_2O$ (Acros Organics, 99%) precursors. Additional synthesis details were described previously.[17] Highly hygroscopic Pr_6O_{11} and La_2O_3 were first pre-fired at 900 °C overnight to remove residual water before weighing targeted precursor mixtures. Final annealing was performed at 1200 °C for 12 h in air, leading to well crystallized phases. The samples were furnace cooled (2 K/min) in static air under identical conditions. As discussed below and shown previously,[48] this leads to larger oxygen δ values for Pr-rich compositions ($\delta = 0.25$ for $x = 2.0$) than for La-rich compositions ($\delta = 0.16$ for $x = 0.0$). One sample of $Pr_2NiO_{4+\delta}$ was also slowly

cooled under an Ar atmosphere ($pO_2 \approx 10^{-4}$ atm) to independently study the structural evolution with lower oxygen δ values (δ = 0.19).

3.2 Structural Analyses

The powders were first characterized by laboratory powder X-ray diffraction (PXRD) at room temperature using a PANanalytical X'pert MPD diffractometer with Cu-Kα source and flat-plate reflection geometry. Most LPNO samples were also measured by high-resolution synchrotron powder diffraction (HR-SPD) at beamline 11-BM of the Advanced Photon Source (APS). HR-SPD measurements were performed at room temperature in a transmission capillary mode using an incident beam energy of 30 keV (λ ≈ 0.41 Å) over the range 0.5 to 50° in 2θ. For the x = 2.0 composition of $Pr_2NiO_{4+\delta}$, *in-situ* variable temperature HR-SPD experiments at 11-BM were also performed from 100 to 450 K to study the structural evolution with temperature. Time of flight neutron powder diffraction (TOF-NPD) data were collected for select LPNO compositions (x = 0.6, 1.2, 1.5 and 2) at 298 K using the POWGEN beamline at the Spallation Neutron Source (SNS). Data obtained via the POWGEN mail-in service were collected on approximately 5 grams of powder loaded into 8.0 mm diameter V cans for approximately 2 hours per sample using the detector banks covering the range 0.4 – 9.0 Å.

Analysis by the Rietveld method for both X-ray and Neutron powder diffraction data (including combined joint refinements of HR-SPD and TOF-NPD data when feasible) were performed using the GSAS/EXPGUI software package.[49,50] Peak profiles for X-ray data were fitted with a pseudo-voigt model incorporating asymmetry due to axial divergence and micro-strain broadening (GSAS Type 4), TOF-NPD profiles have been fit with a convoluted back-to-back exponentials and pseudo-voigt profile (GSAS Type 3). Estimated sample absorption (μR) was considered negligible for both x-ray and neutron datasets. Chebyshev polynomials were used to fit backgrounds. In most cases, lattice parameters, atom positions and anisotropic displacement term values were refined. Profile terms obtained from instrument resolution functions based on refinements of LaB_6 SRM data were fixed, while Lorentzian crystallite size and strain profile terms (including Stephens model type anisotropic microstrain) were refined. Occupancies of interstitial oxygen sites were refined, but with constrained isotropic displacement term values. Other limited refinement constraints, in particular for equivalent Pr and La sites, were employed. Phase weight fractions were refined for the 2-phase region of $0.5 \leq x \leq 1.0$, but with isotropic atomic displacement terms as required to obtain stable refinements. On close inspection of HR-SPD data for most Pr containing samples ($x > 0$), extremely weak impurity peaks assigned to NiO (*Fm*3*m*, a = 4.176 Å) were observed, which refined to approximately 0.1 wt% when included as a secondary phase in trial Rietveld refinements. NiO was therefore excluded from final structure refinements. Resulting crystal structures and difference Fourier maps used to visualize the interstitial oxygen sites were plotted using the VESTA software package.[51]

Electron diffraction analysis of PNO sample was performed using a JEOL 2100 electron microscope. Samples were prepared after grinding under ethanol and crystallites were deposited on a carbon film supported copper grid. Experiments were performed at 100 K, in an attempt to prevent modification of the sample due to beam heating, and also at 300 K. Electron diffraction patterns were obtained by selected area diffraction.

3.3 Additional Characterizations

Thermogravimetric analysis (TGA) was performed to determine oxygen δ values at room temperature. Chemical analyses of La-rich compositions conducted by electron microprobe with approximately 1 μm³ probe size (CAMECA SX 100) confirmed a homogenous distribution of Pr, La and Ni cations in all examined samples. Details of pellet sintering and physical property measurements, including electrical conductivity values determined under air using the four-probe technique, and polarization resistance values obtained by fitting of Nyquist impedance diagrams, have been reported previously.[17]

4. Results and discussion

Initial examinations of $La_{2-x}Pr_xNiO_{4+\delta}$ samples using low resolution lab-based Cu Kα source powder X-ray measurements confirmed the phase purity and crystalline nature of the targeted powder compositions and suggested as a first approximation the existence of a continuous series of orthorhombic type structures (e.g. *Fmmm* or *Bmab*) across the full composition range. This preliminary result agreed with many previously mentioned ambient temperature literature reports on $La_2NiO_{4+\delta}$ and $Pr_2NiO_{4+\delta}$.[23-28,36-41] However, subsequent inspection using higher resolution diffraction probes revealed that the true LPNO structural phase diagram is considerably more complex.

4.1 Monoclinic Pr-rich Region ($1.0 < x \leq 2.0$)

High resolution SPD data collected on Pr-rich samples at 295 K reveal distinct peak splitting clearly visible in certain (*hkl*) reflections such as $\{\bar{2}20\}/\{220\}$, as seen in Fig. 1a (SPD inset) for the LPNO composition with x = 2.0. The data for the $Pr_2NiO_{4+\delta}$ end member with δ ≈ 0.25 are well fit by a monoclinic *F*2/*m* space group with lattice parameters of a ≈ 5.39 Å, b ≈ 5.46 Å, c ≈ 12.45 Å, and γ ≈ 90.07° (see Table 1). This unit cell corresponds extremely well with details of the low temperature monoclinic (LTM) structure for $Pr_2NiO_{4+\delta}$ recently published in a separate investigation by Broux *et al.*,[46] and provides confirming experimental evidence for an ambient temperature monoclinic structural distortion of $Pr_2NiO_{4+\delta}$ first proposed decades ago.[20,34,35] We note that close inspection by monochromatic lab-based Cu $K\alpha_1$ powder X-ray measurements of PNO also suggests a non-orthorhombic distortion, although less distinctly visible than in the HR-SPD datasets.

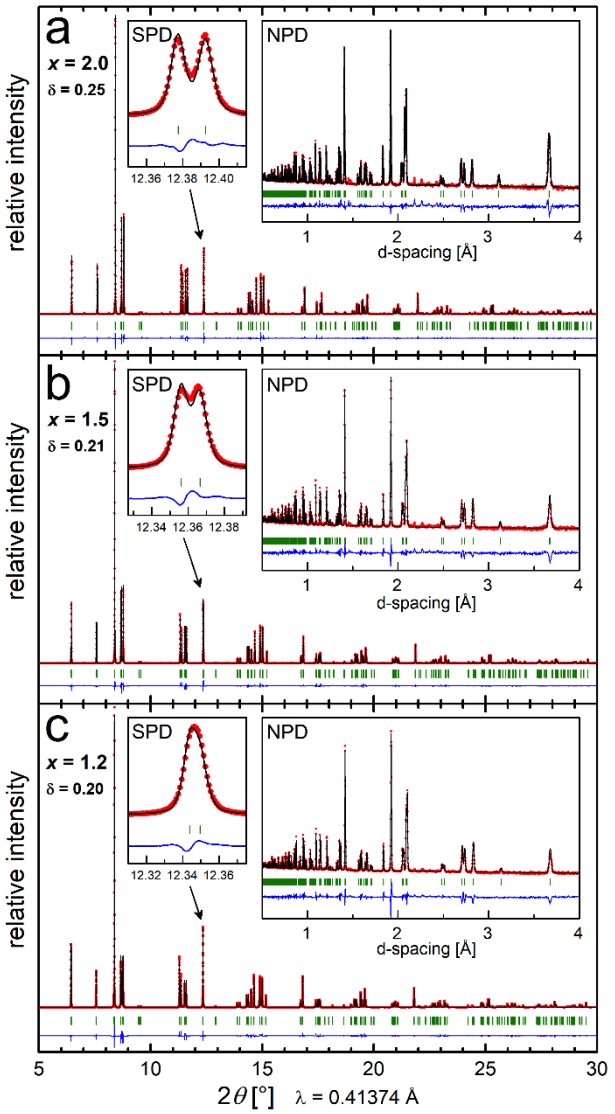

Fig 1 Combined Rietveld refinement fit profiles for $La_{2-x}Pr_xNiO_{4+\delta}$ compositions x = 2.0 (a), 1.5 (b), and 1.2 (c) refined with a monoclinic *F*2/*m* model at 295 K. Small plot inset highlights splitting of {$\bar{2}$20}/{220} reflections in SPD data, large inset shows Rietveld refinement fit profiles of NPD datasets.

The non-standard *F*-centered *F*2/*m* unit cell was selected instead of the more common and equivalent *C*2/*m* setting (space group nº 12) for consistency with previous literature and to facilitate comparison with other orthorhombic and tetragonal structures in the LPNO series. However, as a monoclinic *F*-centered unit cell can always be reduced to a smaller *C*-centered monoclinic cell, the smaller and more strictly crystallographic accurate PNO cell is *C*2/*m* with $a \approx 5.39$ Å, $b \approx 12.45$ Å, $c \approx 3.83$ Å, and $\beta \approx 134.62°$. Supplemental Fig. S1 illustrates the transformation between the two cells. The *F*2/*m* space group is consistent with the parent tetragonal K_2NiF_4-type HTT structure, as there is a direct crystallographic group/subgroup path from tetragonal *I*4/*mmm* (or its equivalent non-standard *F*4/*mmm* setting) space group (nº 139) via orthorhombic *Fmmm* (nº 69) to monoclinic *F*2/*m* (nº 12) as diagrammed in Supplemental Fig. S2.[52] Using nonstandard *F* centered cells helps to maintain common unit cell axes among all subgroups of the tetragonal parent cell.

Rietveld refinements demonstrate that a single *F*2/*m* monoclinic phase provides an excellent fit for Pr-rich LPNO compositions with $1.0 < x \leq 2.0$ at 295 K. This is shown by the refinement difference profiles in Fig. 1 for the compositions x = 2.0, 1.5, and 1.2. The "SPD" plot inset shows a zoomed view of the monoclinic {$\bar{2}$20}/{220} reflection splitting, and the "NPD" plot inset shows fit profiles for complementary NPD-TOF data collected on the same powder sample as part of the combined Rietveld refinement. The monoclinic distortion is diminished by La substitution as highlighted by the reduced {$\bar{2}$20}/{220} splitting in Fig 1. As listed in Table 1, for x = 1.1 the refined monoclinic γ angle is essentially 90°. An overall expansion of the lattice and cell volume is observed with La substitution, consistent with replacing Pr^{3+} by the larger La^{3+} cation (1.179 Å and 1.216 Å for 9-fold coordination, respectively).[53]

For all Pr-rich LPNO compositions, additional weak intensity peaks are seen in both SPD and NPD data which cannot be indexed by a *F*2/*m* cell. Except for minor peaks from NiO mentioned earlier, other likely impurity phase sources have been systematically excluded. The small non-indexed peaks for LPNO compositions with $x > 1.0$ are highlighted in supplemental Figure S3, which plots SPD data sets indexed using a generic orthorhombic *F*-centered cell with a zoomed vertical scale near the background intensity level. This observation of additional non-indexed peaks is consistent with previous literature on $Pr_2NiO_{4+\delta}$ referenced earlier.[10,38-41,46] Also, as shown in Figure 5 and discussed further below, local TEM electron diffraction analysis similarly revealed additional non-indexed reflections. This confirms that these peaks originate from the main LPNO phase. Indexing attempts to find lower symmetry and/or larger volume cells for PNO that could explain all additional observed peaks were unsuccessful. Moreover, none of the unindexed peak positions can be explained by characteristic {212} or {032} reflections associated with long range order of NiO_6 octahedra in-plane tilting as allowed in the space groups such as *Bmab*, *Pccn*, or $P4_2/ncm$ which were previously proposed.

Although the small monoclinic distortion is not detectable in the lower resolution TOF-NPD data, the complementary scattering sensitivity of neutron data in the joint refinements provides greater detail of atomic site positions and displacement parameters. In particular, for single phase Pr-rich monoclinic compositions with $1.0 < x \leq 2.0$ the combined data allow for stable refinements of not only lattice values and atomic positions, but also anisotropic displacements parameters and occupancy of the interstitial oxygen site. Table 1 lists a summary of select refined structural and lattice values for all examined $La_{2-x}Pr_xNiO_{4+\delta}$ compositions. Full details of all refined parameters and fit statistics for these compositions are found in supplemental Table S1. Occupancy of the mixed Pr / La sites were fixed to the chemical composition, as no evidence for cation segregation was found during the refinements or by microprobe analysis. Interstitial oxygen ions (refined using an isotropic displacement parameters) partially occupy the (¼,¼,¼) site, and are clearly visible at this position as missing scattering density in Fourier difference maps if excluded from combined refinements.

Estimated oxygen δ values listed in Table S1 are calculated from refined interstitial oxygen O(4) site occupancies and show good agreement when compared to TGA determined δ values measured for select compositions.

A schematic of the ambient temperature refined monoclinic *F*2/*m* structure for PNO (*x* = 2.0) is shown in Figure 2a, where corner sharing NiO_6 octahedra are separated along the *c* direction of the unit cell by Pr_2O_2 blocks and in which the oxygen interstitial sites are partially occupied. The size of atom ellipsoids for Pr (blue), Ni (grey), and O (red) reflect the refined anisotropic displacement parameters (ADP) at 50% probability. Partially filled open circles represent oxygen interstitial O(4) sites. Refined parameters for other LPNO compositions with *x* > 1.0 show a qualitatively similar structural motif, with decreasing average atomic displacement values for greater La substitution and reduced monoclinic distortion. In general, the refined details for Pr-rich *F*2/*m* structures in this study match well with results recently reported for $Pr_2NiO_{4+\delta}$ by Broux *et al*..[46] As discussed in that work, it is not realistic that the large refined anisotropic atomic displacement values for apical O(1) and equatorial O(2/3) oxygen sites imply significant thermal motion of these ions in the structure – which should be relatively small at 300 K - but more likely represent disordered or incommensurate ion displacements, such as octahedra tilting and/or steric repulsions from the interstitial oxygen site. Several previous reports on LNO and PNO have proposed structural models with split apical oxygen sites,[31,39,41] however it was recently shown by pair distribution function (PDF) analysis of neutron and X-ray powder that ambient temperature disorder of apical oxygen atoms in $La_2NiO_{4.18}$ can be well modeled by anisotropic atomic displacement parameters.[54]

Table 1 Summary of refined structural parameters for select compositions (*x*) in the $La_{2-x}Pr_xNiO_{4+\delta}$ system, see Supplemental Table S1 for complete details of all refined parameters and fit statistics.

(*x*)	space group ◊	δ◆	weight fraction▲	*a* (Å)	*b* (Å)	*c* (Å)	γ (°)	*unit cell volume* (Å^3)
0.0	*F m m m*	0.16	--	5.45985(1)	5.46471(1)	12.6862(2)	90	378.510(1)
0.25	*F* 4 / *m m m*	0.16	--	5.45992(1)	= *a*	12.6582(1)	90	377.351(1)
0.4	*F* 4 / *m m m*	0.16	--	5.45700(1)	= *a*	12.6414(1)	90	376.447(1)
0.5	*F* 2 / *m*	0.17	0.66	5.44209(2)	5.46796(2)	12.6318(3)	90.003(1)	375.888(1)
	F 4 / *m m m*		0.34	5.45492(2)	= *a*	12.6315(2)	90	375.867(2)
0.6	*F* 2 / *m*	0.17	0.76	5.43737(2)	5.46892(2)	12.6195(2)	90.003(2)	375.259(1)
	F 4 / *m m m*		0.24	5.45279(3)	= *a*	12.6207(1)	90	375.251(4)
0.8	*F* 2 / *m*	0.18	0.84	5.42874(1)	5.46962(1)	12.5939(1)	90.005(2)	373.994(1)
	F 4 / *m m m*		0.16	5.44904(2)	= *a*	12.5952(1)	90	373.976(3)
1.0	*F* 2 / *m*	0.19	0.92	5.42111(1)	5.46904(1)	12.5706(2)	90.010(2)	372.695(1)
	F 4 / *m m m*		0.08	5.44482(2)	= *a*	12.5702(1)	90	372.656(1)
1.1	*F* 2 / *m*	0.20	--	5.41771(1)	5.46865(1)	12.5572(2)	90.011(2)	372.036(1)
1.2	*F* 2 / *m*	0.20	--	5.41440(1)	5.46809(1)	12.5443(1)	90.026(2)	371.391(1)
1.5	*F* 2 / *m*	0.21	--	5.40572(1)	5.46422(1)	12.5091(1)	90.047(2)	369.495(1)
2.0	*F* 2 / *m*	0.25	--	5.39172(1)	5.45749(1)	12.4478(1)	90.070(2)	366.278(1)

◊ *F*2/*m* (full name *F*112/*m*) is a non-standard setting of *C*2/*m* (n° 12); F4/mmm is a non-standard *I*4/*mmm* setting (n° 139)

◆ Estimated oxygen δ values determined from TGA and/or Rietveld refinements, see Supplemental Table S1 for details.

▲ Refined phase weight fractions for 2-phase samples.

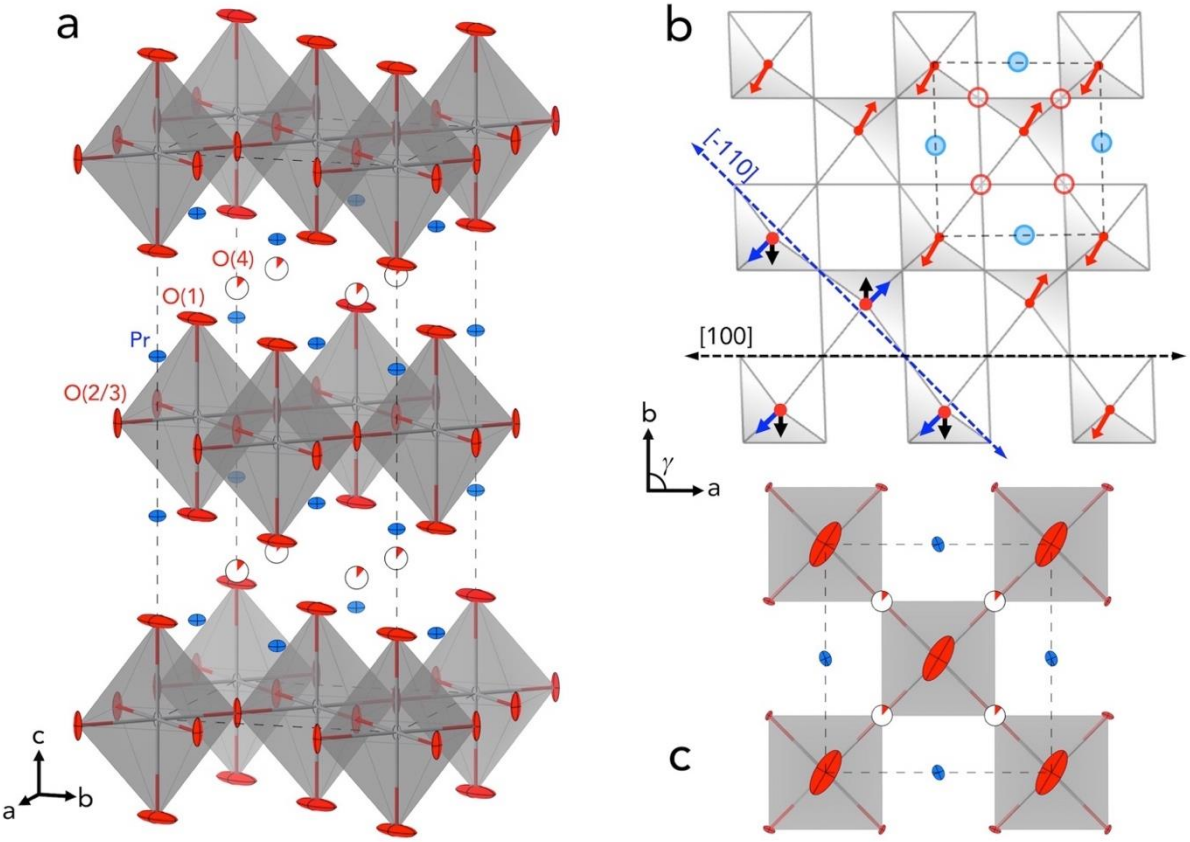

Fig 2 (a) Schematic crystal structure of monoclinic $Pr_2NiO_{4.25}$ at 295 K showing Pr (blue), octahedral Ni (grey), and O (red) sites. Partially occupied O sites are indicated by open circles. (b) Proposed average octahedra tilting schemes (b) may explain the large average oxygen ADP ellipsoids in the refined *F*2/*m* model as viewed along the *c* axis of the unit cell (c). Distortions in (b) are exaggerated for clarity, where the averaged tilting arrangement (red arrows) is composed of non-equivalent tilt components around the [100] and [$\bar{1}$10] unit cell directions (black and blue arrows, respectively).

As discussed by Broux *et al.*,[46] the monoclinic *F*2/*m* cell for Pr-rich compositions likely represents the average structure for an incommensurate ordered or a larger supercell which has not yet been determined. In particular, octahedra tilting arrangements along the *a, b* lattice plane could account for both the large oxygen ellipsoid ADP values and the weak unindexed diffraction peaks. Octahedra tilting arrangements in layered R-P structures have been systematically described previously.[35,55,56] For PNO, tilting may relieve strain from the smaller Pr cation and/or better accommodate interstitial oxygen ions. Figure 2b shows a proposed octahedra tilting arrangement (red arrows) composed of non-equivalent tilt components around the [100] and [$\bar{1}$10] unit cell direction (black and blue arrows, respectively). Pr and interstitial O(4) positions within the unit cell are marked by blue and open red circles, respectively. A long-range modulation of this average NiO_6 octahedra distortion (red arrows) could explain the average oxygen ADP ellipsoids for the refined $Pr_2NiO_{4.25}$ monoclinic *F*2/*m* structure. Using the nomenclature of Aleksandrov,[56] this combination of octahedra tilting could be described as type ($\Phi_1\Phi_2$0), indicating alternating non-equivalent *phi* (Φ_x) tilts with axes of rotation parallel to the *a* and *b* unit cell directions. Incommensurate tilting around the [$\bar{1}$10] direction can account for the subtle monoclinic distortion ($\gamma \neq 90°$) and elongated ADP ellipsoid of the apical oxygen O(1) ions. However, smaller rotations around the [100] direction are only indirectly related to orthorhombic strain ($a \neq b$) observed for the Pr-rich LPNO compositions. Instead, as in other K_2NiF_4 structures,[57] the orthorhombic distortion here is driven primarily by a contraction of Pr/La-O(1) bonds in the *a* direction and the concurrent departure from 90° of the in-plane O-Ni-O bond "scissors" angles. Additional aspects of bonding trends and distortions in the LPNO systems are discussed below.

4.2. Intermediate Mixed Phase Region ($0.5 \leq x \leq 1.0$)

Measured HR-SPD and TOF-NPD data for $La_{2-x}Pr_xNiO_{4+\delta}$ samples with increased La substitution (compositions of $0.5 \leq x \leq 1.0$) are best fit with a mixed 2-phase refinement model. This is illustrated in Fig. 3a, which shows the combined SPD and NPD Rietveld fit profiles for the $x = 0.6$ composition employing a 2-phase mixture of tetragonal *F*4/*mmm* (upper green tick marks) and monoclinic *F*2/*m* (lower brown tick marks) structures. The SPD plot inset in Fig 3a highlights a distinct separation of {113}/{313} and {313} reflections assigned to the monoclinic and tetragonal phases, respectively. In contrast, an equivalent SPD plot inset for the $x = 0.4$ composition in Fig. 3b clearly reveals a single {313} reflection from the tetragonal *F*4/*mmm* unit cell. The evolution of mixed phase $La_{2-x}Pr_xNiO_{4+\delta}$ compositions laying between La-rich single phase tetragonal *F*4/*mmm* ($x = 0.4$) and Pr-rich monoclinic *F*2/*m* ($x = 1.1$) structures can be visualized by examining the varying intensity of {113}/{313} and {313} reflections in Fig. 3c. Refined

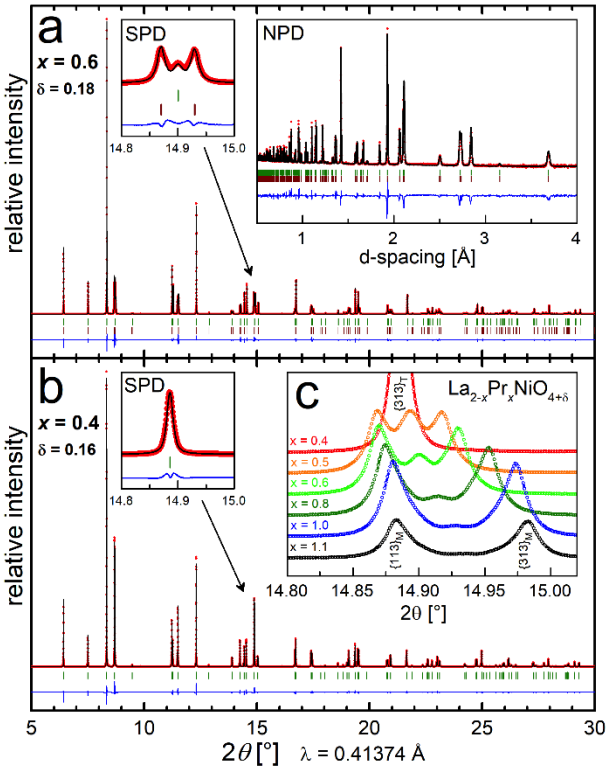

Fig 3 Rietveld refinement profiles for $La_{2-x}Pr_xNiO_{4+\delta}$ compositions, comparing a mixed 2-phase fit for x = 0.6 (a) with a single tetragonal *F*4/*mmm* fit for x = 0.4 (b). Evolution of mixed phase region is tracked by following {113}/{313} and {313} reflections in the HR-SPD data for compositions between $0.4 \leq x \leq 1.1$ (c).

values for this mixed 2-phase region are summarized in Table 1, which includes the refined lattice and weight fraction of both structures for each sample. Full details of refined parameters and fit statistics are found in supplemental Table S1.

Other structural models were considered to fit the diffraction data in this compositional range, such as a lower symmetry single-phase structure, but were ruled out by extensive indexing and refinement analysis. In this compositional range, any peak splitting from a monoclinic distortion is difficult to observe even in the HR-SPD data, but better statistical fits are achieved when the γ angle in the *F*2/*m* phase deviates slightly from 90°. The difference in monoclinic {113}/{313} and tetragonal {313} reflection angular positions highlighted in Figure 3a, in fact arises from the non-equivalent in-plane lattice parameters of the *F*2/*m* ($a \approx 5.43$ Å, $b \approx 5.47$ Å) cell *vs*. the tetragonal *F*4/*mmm* ($a = b \approx 5.45$ Å) cells. This is seen clearly in the plot of LPNO lattice parameters (Figure 4) which also reveals that *c* lattice values are essentially identical for the 2 phases and vary linearly across the entire LPNO series.

Therefore, the primary structural difference in this region is the presence of an orthorhombic-type strain ($a \neq b$) in *F*2/*m* type phases. Due to the overlap of reflections for both phases in the diffraction data, it is impossible to rule out completely a small orthorhombic distortion of the *F*4/*mmm* phases. However, trial two-phase refinements with monoclinic and orthorhombic cells for x = 0.6 and 0.8 did not improve overall fit statistics. Moreover, an orthorhombic cell is inconsistent with refinements of HR-SPD for the La-rich $La_{2-x}Pr_xNiO_{4+\delta}$ compositions (for x = 0.25 and 0.4) which are well fit by single phase tetragonal *F*4/*mmm* cells. Occupancy of the mixed Pr/La sites of each phase were fixed to that of the overall sample composition, as again no evidence for cation segregation was found during the refinements or by microprobe analysis. Moreover, no noticeable differences in refined *c* lattice values, expected from phases with dissimilar Pr/La composition, were observed. We also noted the absence of any weak non-indexed peaks in the HR-SPD for these LPNO compositions, as demonstrated in supplemental Figure S3.

Intermediate $La_{2-x}Pr_xNiO_{4+\delta}$ compositions ($0.5 \leq x \leq 1.0$) therefore apparently lack the complex incommensurate ordering of Pr-rich samples, but segregate into two structural motifs distinguished essentially by non-equivalent orthorhombic-type strain in the *a*-*b* plane. It is possible that this segregation is connected to oxygen interstitial uptake, with distinct accommodation values and/or configurations more stable than an average intermediate arrangement. Differences in the lattice parameters might be expected for phases with identical Pr/La composition but non-equivalent interstitial oxygen δ content, with a larger δ leading to a unit cell expansion along the *c* direction of layer stacking, as seen in $La_2NiO_{4+\delta}$ for $\delta \lesssim 0.16$.[25] However, for higher oxygen content, reported *c* lattice values are relatively constant (≈ 12.70 Å) for $0.16 < \delta < 0.30$.[30,32,58] This suggests oxygen excess at higher concentrations can be accommodated not only by a simple expansion of intra-slab spacing, but instead by different in-plane distortions associated with *a*-*b* orthorhombic-type strain. Note that physical analyses by TGA would give only average oxygen δ values for the ensemble mixture, and that it is not statistically feasible to refine separate interstitial oxygen occupancies in the Rietveld analysis. Examples of mixed orthorhombic and tetragonal phase driven by interstitial oxygen ion segregation in K_2NiF_4-type R-P systems have already been reported previously. Jorgensen *et al*. proposed this behavior for $La_2CuO_{4+\delta}$, where only one of the phases exhibited superconductivity.[59] In $La_2NiO_{4+\delta}$ mixed regions of tetragonal *F*4/*mmm* or $P4_2/ncm$ and orthorhombic *Bmab*-type structures are observed for intermediate oxygen values ($0.02 < \delta < 0.14$).[23-26] Similar behavior is also reported for the $Nd_2NiO_{4+\delta}$ system.[60]

4.3. La-rich Region ($0.0 \leq x < 0.5$)

La-rich $La_{2-x}Pr_xNiO_{4+\delta}$ compositions for $x < 0.5$ are found to be monophasic, with the HR-SPD data best fit by a tetragonal *F*4/*mmm* unit cell for x = 0.25 and x = 0.4 (Figure 3b shows Rietveld refinement difference profile for x = 0.4). No clear orthorhombic type peak distortions are observed on close inspection of the HR-SPD data, and trial refinements using an orthorhombic cell for the x = 0.25 composition did not show meaningful statistical fit improvement (*e.g.* R_{wp} of 11% *vs.* 10%). Depending on temperature and interstitial oxygen δ values, similar LTT tetragonal (F4/*mmm* or $P4_2/ncm$) structures have been reported for $La_2NiO_{4+\delta}$ (in the range $0.06 < \delta < 0.15$),[24,25] $Pr_2NiO_{4+\delta}$ [40] and $Nd_2NiO_{4+\delta}$.[60] An orthorhombic *Fmmm* structure is proposed for the x = 0.0 LPNO end member with δ = 0.16. The refined orthorhombic distortion is quite small (approximately

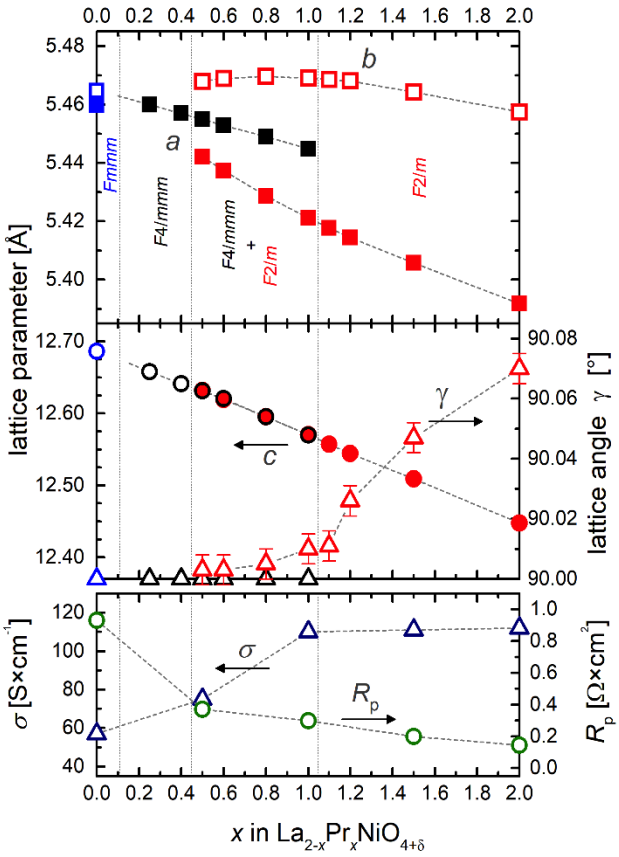

Fig 4 Refined lattice parameters *vs*. composition (*x*) for $La_{2-x}Pr_xNiO_{4+\delta}$ at 295 K, with values for *F*2/*m*, *F*4/*mmm*, and *Fmmm* space groups plotted in red, black and blue, respectively (upper plots). $La_{2-x}Pr_xNiO_{4+\delta}$ compositional dependence at 600 °C of electrical conductivity (σ) and polarization resistance (R_p) taken from Vibhu *et al*. [17] (lower plot) Note dashed lines are a visual guide and certain error bars are smaller than plotted data points.

0.1% difference in *a* and *b* lattice values) and is consistent with previous literature on the well-studied $La_2NiO_{4+\delta}$ compound.[25,31]

4.4 Evolution of non-indexed peaks in Pr-rich compositions

As discussed above in section *4.1*, several weak intensity peaks are seen in both SPD and NPD data for Pr-rich $La_{2-x}Pr_xNiO_{4+\delta}$ compositions ($1.0 < x \leq 2.0$) which cannot be indexed by a *F*2/*m* cell. Similar observations have been made in previous literature on PNO, [10,38-41,46] and Broux *et al.* recently discussed how they could be explained by disordered or incommensurate distortions of the average monoclinic cell.[46]

In the current study, these non-indexed peaks are examined as a function of La/Pr composition (*x*), temperature, and interstitial oxygen content (δ). Figures 5a and 5b plot a narrow 2θ range near the indexed {220} and {222} reflections (partially transparent) in the HR-SPD datasets. In Fig. 5a, the intensity of non-indexed peaks clearly diminishes for decreasing *x* (and δ) and are absent in the mixed phase *x* = 1.0 composition. Note that all peaks shift together toward smaller 2θ values as the average unit cell expands with La substitution, and that monoclinic splitting observed in {222} peaks is decreasing. In Figure 5b, *in-situ* variable temperature HR-SPD data measured between 100 and 450 K for the PNO composition with *x* = 2.0 are displayed as a stacked contour plot over the same 2θ range. Again, all peaks shift together towards smaller 2θ values as the average unit cell expands with increasing temperature, but no other notable changes are observed. TEM electron diffraction recorded at 300 K (Fig 5c) and 100 K (Fig. 5d) on the *x* = 2.0 sample similarly show extra non-indexed reflections marked by red arrows for both temperatures. In combination with separate results of Broux *et al.* collected over a higher temperature range, this suggests that undetermined supercell ordering for over-oxygenated Pr-rich $La_{2-x}Pr_xNiO_{4+\delta}$ structures may exist from 100 K to nearly 1000 K.[46] Monoclinic (*F*2/*m*) unit cell parameters refined against the variable temperature data in this study for $Pr_2NiO_{4.25}$ are plotted in supplemental Figure S4.

Correlations between supercell ordering, Pr/La composition, and interstitial oxygen content, were examined in Pr-rich samples by considering the intensity of non-indexed weak peaks in the HR-SPD data. This qualitative analysis is summarized in Supplemental Figure S5. It assumed that the relative fraction of normalized integrated peak area is proportional to the ordering extent. The integrated peak area of a representative non-indexed peak (at 2θ ≈ 10.88°) was defined as 1.0 for δ = 0.25 and was normalized for each scan as a fraction of the integrated area for the indexed (004) peak at 2θ ≈ 7.60°. The small inset of Fig S5 plots the evolution of this non-indexed peak for air-cooled compositions. In the main plot, red diamonds show air-cooled samples, while the blue diamond represents the Ar-cooled *x* = 2.0 sample with reduced δ (see Supplemental Table S1 for details of refined parameters). The dashed black curve is a guide for the eye. Note that oxygen over-stoichiometry (δ) values were determined by TGA measurements and/or Rietveld analysis of NPD data.

As discussed previously, with decreasing δ and *x*, the extent of supercell ordering decreases, and is absent for $x \leq 1.0$ and/or $\delta \leq 0.19$. This is concurrent with the boundary of the single phase *F*2/*m* region. However, the estimated ordering fraction for the PNO *x* = 2.0 Ar cooled sample is much less than that found in the air-cooled *x* = 2.0 sample, despite very similar refined lattice parameters and monoclinic distortions (γ ≈ 90.06° and 90.07°, respectively). This suggests that supercell ordering in LPNO compositions is more strongly correlated with interstitial oxygen content (δ) than with Pr/La content or average lattice strain. Moreover, it suggests that monoclinic strain in oxygenated Pr-rich compositions of $La_{2-x}Pr_xNiO_{4+\delta}$ is driven primarily by the smaller Pr cation size. The possibility that a "minimum" oxygen δ is required for supercell ordering in Pr-rich LPNO compositions is consistent with the work of Demourgues *et al*. on highly oxygenated $La_2NiO_{4+\delta}$ samples.[30] The complete structural model for PNO and Pr-rich compositions is likely quite complex, as demonstrated for isostructural $La_2CoO_{4.14}$,[61] and any full understanding will require

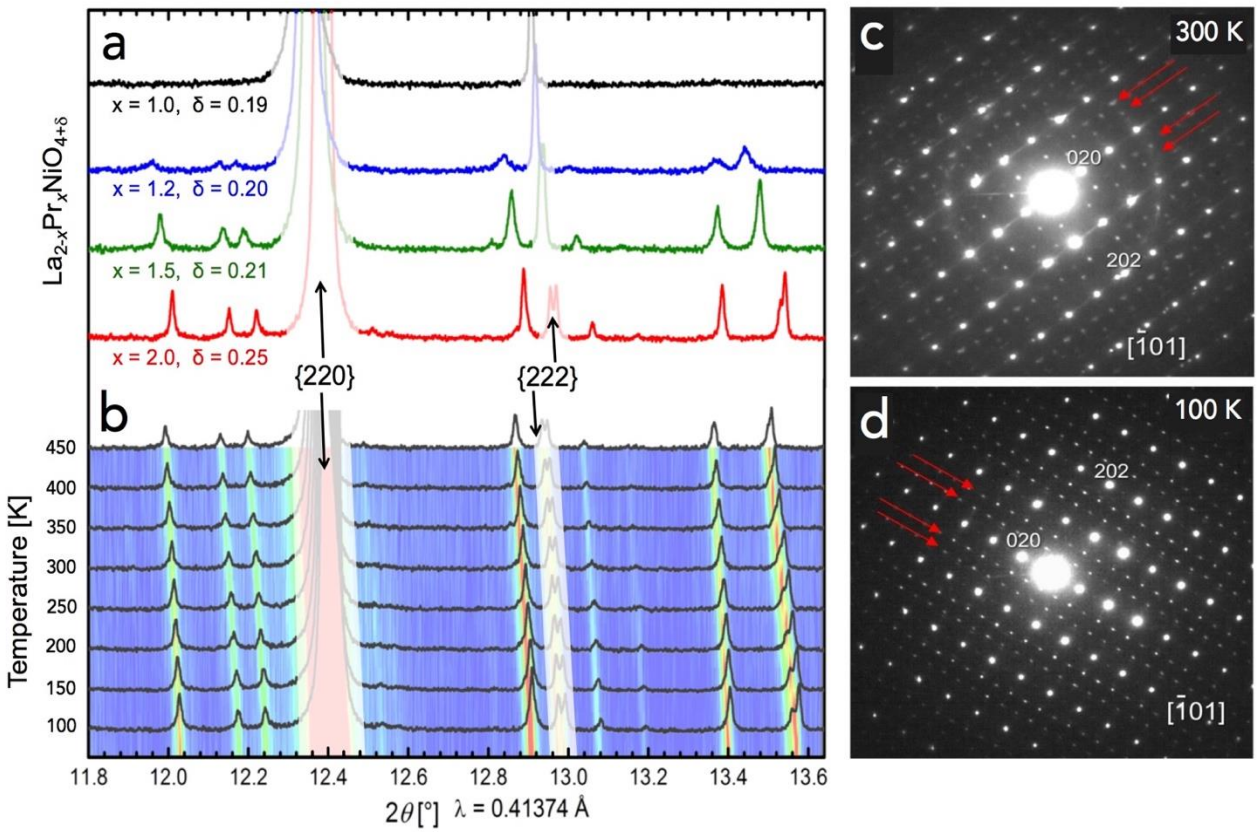

Fig 5 Evolution of non-indexed weak intensity peaks observed in HR-SPD data for (a) selected $La_{2-x}Pr_xNiO_{4+\delta}$ compositions at 295 K, and (b) for $Pr_2NiO_{4.25}$ as a function of temperature from 100 K to 450 K. TEM electron diffraction at (c) 300 K and (d) 100 K showing extra non-indexed reflections marked by red arrows visible at both temperatures for the x = 2.0 composition.

additional single crystal studies similar to those published by Ceretti *et al.* on $Nd_2NiO_{4+\delta}$ and $Pr_2NiO_{4+\delta}$.[45]

4.5 Structure and property trends in $La_{2-x}Pr_xNiO_{4+\delta}$

Refined lattice parameters from the LPNO series are plotted in Figure 4, showing trends across the monoclinic Pr-rich ($1.0 < x \leq 2.0$), intermediate mixed phase ($0.5 \leq x \leq 1.0$), and single-phase La-rich ($0.0 \leq x < 0.5$) regions. This adds considerable new detail to previous investigations which reported only orthorhombic structures across the $La_{2-x}Pr_xNiO_{4+\delta}$ (LPNO) series.[15-19,48] A lower resolution diffraction study of the related $La_{2-x}Nd_xNiO_{4+\delta}$ system reports similar trends, with quasi-tetragonal La-rich compositions and smaller orthorhombically strained Nd-rich unit cells.[62] It is possible that future studies of the $La_{2-x}Nd_xNiO_{4+\delta}$ system will reveal additional complexity analogous to that observed in this current study.

An inspection of cation-oxygen bond distances in the LPNO series helps to give insight into the observed average structural changes. Figure 6 displays selected Pr/La-O and Ni-O bond lengths extracted from structural models refined using the 295 K diffraction data. Schematics of the first shell cation-oxygen bonding environment for Pr/La (top) and Ni (bottom) highlight (green arrows) the most significant bond contractions in the monoclinic $Pr_2NiO_{4.25}$ (x = 2.0) structure, as compared to the larger and highest symmetry unit cell (*F*4/*mmm*) of La-rich compositions of $x < 0.4$. Tabulated values of the bond distances are given in Supplemental Table S3.

Strain associated with the replacement of La^{3+} by the smaller Pr^{3+} drives distortions in this system. This approximate 3% decrease in ionic cation radii gives rise to a roughly equivalent compression of intra-slab spacing along the *c* direction, which is significantly accommodated by a shrinking of the shortest La/Pr – apical O(1) bond (≈ 2.35 Å) along the same direction. Distinctly non-equivalent contraction of La/Pr-O bonds (≈ 2.75 Å) along the *a*-*b* plane produces the orthorhombic strain ($a \neq b$) observed for pseudo-monoclinic structures in the mixed phase region of LPNO (and splits the equatorial O(2/3) site). It is speculated that segregation of average structures in the intermediate mixed phase region is connected to oxygen interstitial uptake, with distinct accommodation values and/or configurations more stable than an average intermediate arrangement. The energetically favorable insertion of interstitial oxygen between slab layers reduces overall strain and explains the trend of higher δ values (for equivalent annealing) of Pr-rich compositions. But the effect of excess oxygen insertion on overall unit cell volume is also partially offset by a smaller $Ni^{2+/3+}$ cation radius with increased oxidation.

NiO_6 octahedra are more rigid and show a slight uniaxial compression with moderate Pr substitution. In-plane Ni equatorial O(2/3) bonds are relatively constant across the series

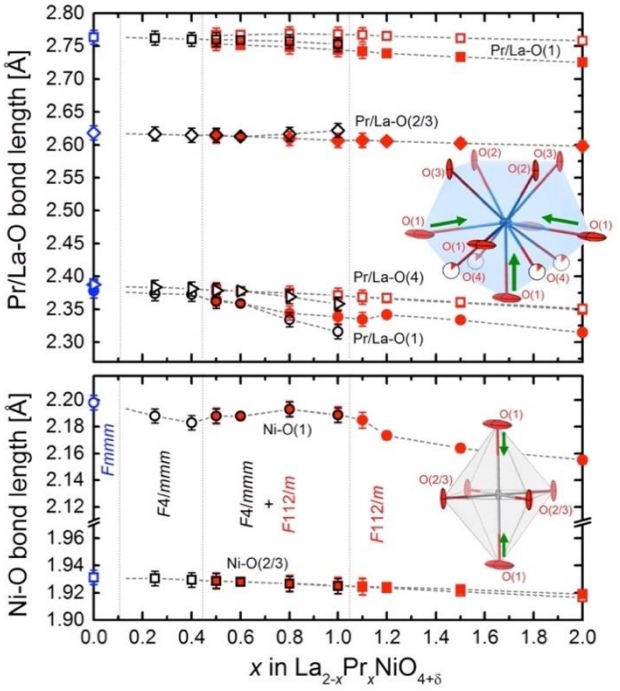

Fig 6 Selected Pr/La-O (top) and Ni-O (bottom) bond lengths at 295 K *vs*. composition (*x*) in $La_{2-x}Pr_xNiO_{4+\delta}$. Inset graphics illustrate bonding around Pr/La site (blue ellipsoid at top) and Ni site (grey ellipsoid at bottom). Dashed lines are a guide for the eye.

despite the non 90° O-Ni-O bond "scissors" angles associated with orthorhombic strain. In contrast, Ni apical O(1) bonds (≈ 2.18 Å) exhibit a discreet trend of increasing contraction for Pr-rich compositions ($x > 1$) concurrent with the growth of the average monoclinic distortion ($\gamma \neq 90°$). As discussed previously, the refined *F*2/*m* monoclinic structure of Pr-rich compositions likely represents the average of more complex tilting arrangement with short correlation lengths and/or incommensurate ordering. However, the extent of supercell ordering evidenced by weak peaks in LPNO compositions appears to be more strongly correlated with interstitial oxygen content (δ) than with Pr/La content or average lattice distortion.

Promising electrochemical properties of the PNO end member ($x = 2.0$) are undermined by poor chemical stability at elevated temperatures corresponding to SOFC operating conditions.[10-14,18] The monoclinic distortion and supercell ordering seen at ambient temperature here may therefore reflect a highly strained structure that readily decomposes to more thermodynamically stable compositions. However, good electrochemical performance is maintained with partial La substitutions ($x \leq 0.5$). As shown in Figure 4c, the electrical conductivity (σ) for $La_{2-x}Pr_xNiO4_{+\delta}$ compositions increases with *x* (data collected at 600 °C, taken from Vibhu *et al.*[17]) since the polarization resistance (R_p) significantly decreases. Based on thermal stability with ageing, we have shown that the $x = 0.5$ composition, which is the limit of the La-rich LPNO single-phase domain, is the best compromise between performance and thermal stability for these SOFC cathode materials. However, it is noted that a somewhat different result has been recently reported for materials with the same nominal compositions but quite different shaping (thin films).[19,63] For these thin film studies, the ideal compromise of $La_{2-x}Pr_xNiO4_{+\delta}$ performance and stability is reported at $x = 1.0$. However, in bulk ceramics, this more Pr-rich composition is unstable at operating temperatures *vs.* time.[18]

4. Conclusions

A detailed structural study of the $La_{2-x}Pr_xNiO_{4+\delta}$ system, which is of interest for cathode materials in solid oxide fuel cells, has been performed using high resolution synchrotron and neutron powder diffraction data. This has enabled an investigation of average distortions and cation-oxygen bond bonding as a function of composition, temperature and oxygen over-stoichiometry. Diffraction data for Pr-rich compositions ($1.0 < x \leq 2.0$) reveal a monoclinic distortion (*F*2/*m*), large ellipsoidal ADP values, and weak supercell peaks which likely represent as-of-yet undetermined octahedra tilt arrangements and/or long-range structural modulations. It is proposed that supercell ordering is more intimately associated with interstitial oxygen content than average unit cell strain. Both features are preserved over the temperature range of 100 - 450 K. In compositions with increasing La substitution ($0.5 \leq x \leq 1.0$), a region of mixed tetragonal and pseudo-monoclinic phases is described, interpreted as local segregation into different oxygen interstitial related structural motifs primarily distinguished by non-equivalent orthorhombic-type strain in the *a*-*b* plane. La-rich compositions are found to be single phase tetragonal (*F*4/*mmm* for $0 < x < 0.5$) or orthorhombic (*Fmmm* for $x = 0$) and consistent with previous reports.

A more complete understanding of possible supercell and/or modulations in the Pr-rich $La_{2-x}Pr_xNiO_{4+\delta}$ compositions will certainly require further detailed studies of single crystal diffraction data. Likewise, details of the mixed phase region might be better resolved with additional examinations of possible compositional segregations varying as a function of average oxygen δ values and annealing conditions. Finally, it is suggested that a high-resolution examination of the analogous $La_{2-x}Nd_xNiO_{4+\delta}$ system may reveal similar complexity to that observed in the current study.

Conflicts of interest

There are no conflicts to declare.

Acknowledgements

The authors wish to acknowledge gratefully the Agence Nationale de la Recherche (A.N.R., France, PEREN Project; ANR-2011-PREG-016-05) for financial support. This work used resources at the Spallation Neutron Source, a DOE Office of Science User Facility operated by the Oak Ridge National Laboratory. Use of the Advanced Photon Source at Argonne National Laboratory was supported by the U. S. Department of Energy, Office of Science, Office of Basic Energy Sciences, under Contract No. DE-AC02-06CH11357

References

1 A. Tarancón, M. Burriel, J. Santiso, S. J. Skinner and J. A. Kilner, *J. Mater. Chem.*, 2010, **20**, 3799–3813.

2 C. Sun, R. Hui and J. Roller, *J. Solid State Electrochem.*, 2010, **14**, 1125–1144.

3 A. J. Jacobson, *Chem. Mater.*, 2010, **22**, 660–674.

4 D. J. L. Brett, A. Atkinson, N. P. Brandon and S. J. Skinner, *Chem. Soc. Rev.*, 2008, **37**, 1568–1578.

5 J.-C. Grenier, J.-M. Bassat and F. Mauvy, in *Functional Materials for Sustainable Energy Applications*, eds. J. A. Kilner, S. J. Skinner, S. J. C. Irvine and P. P. Edwards, 2014, vol. 1, pp. 402–444.

6 A. Chroneos, D. Parfitt, J. A. Kilner and R. W. Grimes, *J. Mater. Chem.*, 2010, **20**, 266–270.

7 Z. Gao, L. V. Mogni, E. C. Miller, J. G. Railsback and S. A. Barnett, *Energy Environ. Sci.*, 2016, **9**, 1602–1644.

8 E. Boehm, J.-M. Bassat, P. Dordor, F. Mauvy and J.-C. Grenier, *Solid State Ionics*, 2005, **176**, 2717–2725.

9 C. Ferchaud, J.-C. Grenier, Y. Zhang-Steenwinkel, M. M. A. van Tuel, F. P. F. van Berkel and J.-M. Bassat, *J. Power Sources*, 2011, **196**, 1872–1879.

10 J. D. Sullivan, D. J. Buttrey, D. E. Cox and J. Hriljac, *J. Solid State Chem.*, 1991, **94**, 337–351.

11 P. Odier, C. Allançon and J.-M. Bassat, *J. Solid State Chem.*, 2000, **153**, 381–385.

12 A. V. Kovalevsky, V. V. Kharton, A. A. Yaremchenko, Y. V. Pivak, E. V. Tsipis, S. O. Yakovlev, A. A. Markov, E. N. Naumovich and J. R. Frade, *J of Electroceramics*, 2007, **18**, 205–218.

13 V. Vibhu, A. Rougier, C. Nicollet, A. Flura, S. Fourcade, N. Penin, J.-C. Grenier and J.-M. Bassat, *J. Power Sources*, 2016, **317**, 184–193.

14 J.-M. Bassat, V. Vibhu, C. Nicollet, A. Flura, S. Fourcade, J.-C. Grenier and A. Rougier, *ECS Transactions*, 2017, **78**, 655–665.

15 G. T. Kim and A. J. Jacobson, *Mater. Res. Soc. Symp. Proc.*, 2006, **972**, AA11–04.

16 S. Nishimoto, S. Takahashi, Y. Kameshima, M. Matsuda and M. Miyake, *J. Ceram. Soc. Jpn.*, 2011, **119**, 246–250.

17 V. Vibhu, A. Rougier, C. Nicollet, A. Flura, J.-C. Grenier and J.-M. Bassat, *Solid State Ionics*, 2015, **278**, 32–37.

18 V. Vibhu, J.-M. Bassat, A. Flura, C. Nicollet, J.-C. Grenier and A. Rougier, *ECS Transactions*, 2015, **68**, 825–835.

19 R. K. Sharma, S.-K. Cheah, M. Burriel, L. Dessemond, J.-M. Bassat and E. Djurado, *Journal of Materials Chemistry A*, 2017, **5**, 1120–1132.

20 K. K. Singh, P. Ganguly and J. B. Goodenough, *J. Solid State Chem.*, 1984, **52**, 254–273.

21 D. J. Buttrey and J. M. Honig, in *Chemistry of High Temperature Superconductors*, ed. C. N. R. Rao, 1991, pp. 283–305, ISBN: 978-981-02-0805-9.

22 H. Takagi, S.-I. Uchida, K. Kitazawa and S. Tanaka, *Jpn. J. Appl. Phys.*, 1987, **26**, L123.

23 J. D. Jorgensen, B. Dabrowski, S. Pei, D. R. Richards and D. G. Hinks, *Phys. Rev. B: Condens. Matter*, 1989, **40**, 2187–2199.

24 J. Rodriguez-Carvajal, M. T. Fernández-Díaz and J. L. Martinez, *J Phys-Condens Mat*, 1991, **3**, 3215–3234.

25 D. E. Rice and D. J. Buttrey, *J. Solid State Chem.*, 1993, **105**, 197–210.

26 J. M. Tranquada, Y. Kong, J. E. Lorenzo, D. J. Buttrey, D. E. Rice and V. Sachan, *Phys. Rev. B*, 1994, **50**, 6340–6351.

27 H. Tamura, A. Hayashi and Y. Ueda, *Physica C*, 1996, **258**, 61–71.

28 H. Tamura, A. Hayashi and Y. Ueda, *Physica C*, 1993, **216**, 83–88.

29 A. Demourgues, F. Weill, B. Darriet, A. Wattiaux, J.-C. Grenier, P. Gravereau and M. Pouchard, *J. Solid State Chem.*, 1993, **106**, 317–329.

30 A. Demourgues, A. Wattiaux, J.-C. Grenier, M. Pouchard, J. L. Soubeyroux, J. M. Dance and P. Hagenmuller, *J. Solid State Chem.*, 1993, **105**, 458–468.

31 S. J. Skinner, *Solid State Sciences*, 2003, **5**, 419–426.

32 A. Aguadero, J. A. Alonso, M. J. Martinez-Lope, M. T. Fernandez-Diaz, M. J. Escudero and L. Daza, *J. Mater. Chem.*, 2006, **16**, 3402–3408.

33 A. Flura, S. Dru, C. Nicollet, V. Vibhu, S. Fourcade, E. Lebraud, A. Rougier, J.-M. Bassat and J.-C. Grenier, *J. Solid State Chem.*, 2015, **228**, 189–198.

34 B. Willer and M. Daire, *C. R. Acad. Sci., Ser. C: Sci. Chim.*, 1968, **267**, 1482–1484.

35 P. Ganguly and C. N. R. Rao, *J. Solid State Chem.*, 1984, **53**, 193–216.

36 R. S. Puche, F. Fernández, J. Rodríguez-Carvajal and J. L. Martinez, *Solid State Commun.*, 1989, **72**, 273–277.

37 J. L. Martinez, M. T. Fernandez-Diaz, J. Rodriguez-Carvajal and P. Odier, *Phys. Rev. B*, 1991, **43**, 13766–13769.

38 M. T. Fernandez-Diaz, J. Rodriguez-Carvajal, J. L. Martinez, G. Fillion, F. Fernanadez and R. Saez-Puche, *Z. Phys. B: Condens. Matter*, 1991, **82**, 275–282.

39 M. T. Fernandez-Diaz, J. L. Martinez and J. Rodriguez-Carvajal, *Solid State Ionics*, 1993, **63-65**, 902–906.

40 C. Allançon, A. Gonthier-Vassal, J.-M. Bassat, J. P. Loup and P. Odier, *Solid State Ionics*, 1994, **74**, 1239–1248.

41 C. Allançon, J. Rodríguez-Carvajal, M. T. Fernandez-Diaz, P. Odier, J.-M. Bassat, J. P. Loup and J. L. Martinez, *Z. Phys. B: Condens. Matter*, 1996, **100**, 85–90.

42 M. Yashima, M. Enoki, T. Wakita, R. Ali, Y. Matsushita, F. Izumi and T. Ishihara, *J. Am. Chem. Soc.*, 2008, **130**, 2762–2763.

43 D. Parfitt, A. Chroneos, J. A. Kilner and R. W. Grimes, *Phys. Chem. Chem. Phys*, 2010, **12**, 6834–3.

44 J.-M. Bassat, M. Burriel, O. Wahyudi, R. Castaing, M. Ceretti, P. Veber, I. Weill, A. Villesuzanne, J.-C. Grenier, W. Paulus and J. A. Kilner, *J. Phys.Chem C.*, 2013, **117**, 26466–26472.

45 M. Ceretti, O. Wahyudi, A. Cousson, A. Villesuzanne, M. Meven, B. Pedersen, J.-M. Bassat and W. Paulus, *Journal of Materials Chemistry A*, 2015, **3**, 21140–21148.

46 T. Broux, C. Prestipino, M. Bahout, S. Paofai, E. Elkaïm, V. Vibhu, J.-C. Grenier, A. Rougier, J.-M. Bassat and O. Hernandez, *Dalton Transactions*, 2016, **45**, 3024–3033.

47 E. Dogdibegovic, Q. Cai, N. S. Alabri, W. Guan and X.-D. Zhou, *J. Electrochem. Soc.*, 2017, **164**, F99–F106.

48 C. Allançon, P. Odier, J.-M. Bassat and J. P. Loup, *J. Solid State Chem.*, 1997, **131**, 167–172.

49 B. H. Toby, *J Appl Crystallogr*, 2001, **34**, 210–213.

50 A. C. Larson and R. B. Von Dreele, *GSAS. Report LAUR 86-748*, Los Alamos National Laboratory, New Mexico, USA., 2004.

51 K. Momma and F. Izumi, *J Appl Crystallogr*, 2011, **44**, 1272–1276.

52 M. I. Aroyo, A. Kirov, C. Capillas, J. M. Perez-Mato and H. Wondratschek, *Acta Crystallogr., Sect. A*, 2006, **62**, 115–128.

53 R. D. Shannon, *Acta Crystallogr., Sect. A*, 1976, **32**, 751–767.

54 M. Brunelli, M. Coduri, M. Ceretti and W. Paulus, *J. Phys. D: Appl. Phys.*, 2015, **48**, 504009.

55 K. S. Aleksandrov and J. Bartolome, *J Phys-Condens Mat*, 1994, **6**, 8219–8235.

56 K. S. Aleksandrov, B. V. Beznosikov and S. V. Misyul, *Phys. Status Solidi A*, 1987, **104**, 529–543.
57 P. Radaelli, D. Hinks, A. Mitchell, B. Hunter, J. Wagner, B. Dabrowski, K. Vandervoort, H. Viswanathan and J. Jorgensen, *Phys. Rev. B*, 1994, **49**, 4163–4175.
58 A. Aguadero, M. Pérez, J. A. Alonso and L. Daza, *J. Power Sources*, 2005, **151**, 52–56.
59 J. Jorgensen, B. Dabrowski, S. Pei, D. Hinks, L. Soderholm, B. Morosin, J. Schirber, E. Venturini and D. Ginley, *Phys. Rev. B: Condens. Matter*, 1988, **38**, 11337–11345.
60 K. Ishikawa, K. Metoki and H. Miyamoto, *J. Solid State Chem.*, 2009, **182**, 2096–2103.
61 L. Le Dréau, C. Prestipino, O. Hernandez, J. Schefer, G. Vaughan, S. Paofai, J. M. Perez-Mato, S. Hosoya and W. Paulus, *Inorg. Chem*, 2012, **51**, 9789–9798.
62 H. Ishikawa, Y. Toyosumi and K. Ishikawa, *J Alloy Compd*, 2006, **408-412**, 1196–1199.
63 R. K. Sharma, O. Celikbilek, M. Burriel, L. Dessemond, J.-M. Bassat and E. Djurado, *ECS Transactions*, 2016, **72**, 1–8.

Supplemental Information

Structural transformations of the $La_{2-x}Pr_xNiO_{4+\delta}$ system probed by high-resolution synchrotron and neutron powder diffraction

Vaibhav Vibhu [a,b], Matthew R. Suchomel †[a,b], Nicolas Penin [a,b], François Weill [a,b], Jean-Claude Grenier [a,b], Jean-Marc Bassat [a,b], and Aline Rougier [a,b]

[a.] *CNRS, ICMCB, UMR 5026, F-33600 Pessac, France*
[b.] *Univ. Bordeaux, ICMCB, UMR 5026, F-33600 Pessac, France*
† Corresponding author

Transformation from expanded F2/m monoclinic cell to standard *C*2/*m* monoclinic cell
(Space Group #12, Setting: C 1 2/*m* 1)

*F*2/*m* → *C*2/*m*

$$\begin{bmatrix} a \\ b \\ c \end{bmatrix} \begin{bmatrix} -1 & 0 & 0 \\ 0 & 0 & 1 \\ 1/2 & 1/2 & 0 \end{bmatrix} = \begin{bmatrix} a' \\ b' \\ c' \end{bmatrix}$$

Transformation for $Pr_2NiO_{4.25}$

*F*2/*m*	→	*C*2/*m*
a = 5.3917 Å		*a*′ = 5.3917 Å
b = 5.4574 Å		*b*′ = 12.4478 Å
c = 12.4478 Å		*c*′ = 3.8335 Å
γ = 90.07 °		*β*′ = 134.62 °
V = 366.27 Å^3		V′ = $V/_2$ = 183.13 Å^3
Pr @ (0, 0, 0.36)		Pr @ (0, 0.36, 0)
Ni @ (0, 0, 0)		Ni @ (0, 0, 0)
O1 @ (0, 0, 0.17)		O1 @ (0, 0.17, 0)
O2 @ (¼, ¼, 0)		O2 @ (0, 0, ½)
O3 @ (¾, ¼, 0)		O3 @ (½, 0, ½)
O4 @ (¼, ¼, ¼)		O4 @ (0, ¼, ½)

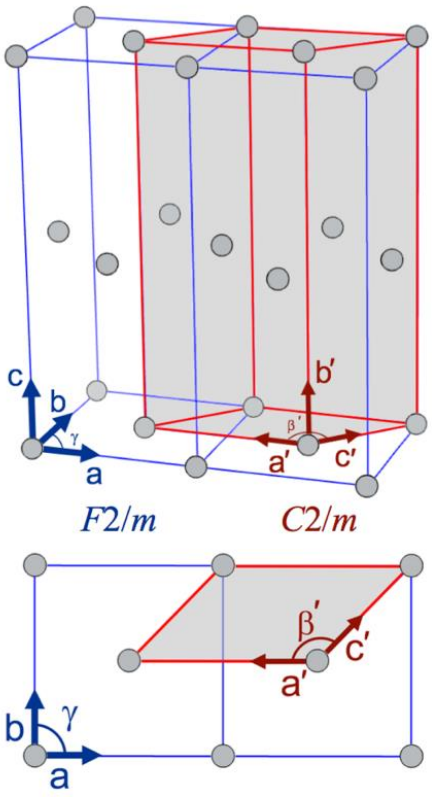

Supplemental Figure S1: Relationship between expanded *F*2/*m* monoclinic unit cell (full name *F*112/*m* with unique axis c) used in this work and its equivalent reduced conventional *C*2/*m* cell in its standard crystallographic setting (full name *C*12/*m*1 with unique axis *b*). On the left, the transformation matrix is given, and corresponding lattice values and atomic positions are given for the $Pr_2NiO_{4.25}$ composition. On the right, a schematic diagram of the relationship between the *F*2/*m* cell (in blue) and *C*2/*m* cell (in red) is shown. For clarity, only the Ni atom is plotted in the unit cell.

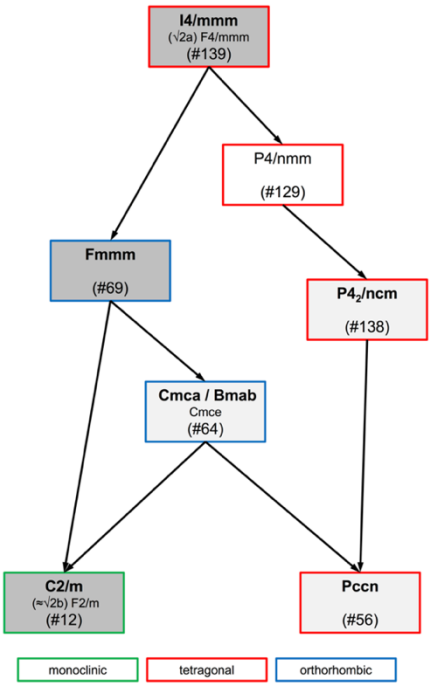

Supplemental Figure S2: Selected group/subgroup relationship paths between different space groups commonly referenced in the $La_2NiO_{4+\delta}$ and $Pr_2NiO_{4+\delta}$ literature; from the Bilbao Crystallographic Server [52]. Shaded space groups are reported for the LPNO system in the current study.

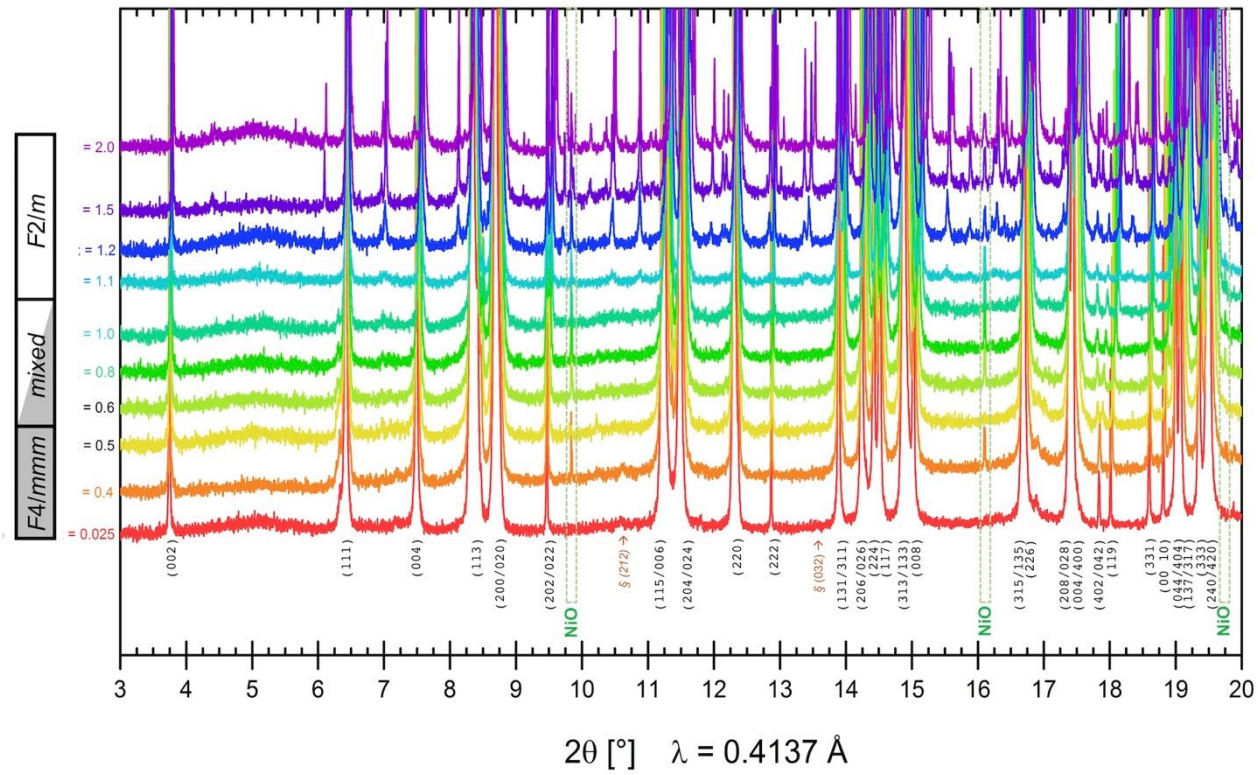

Supplemental Figure S3: Near background intensity zoomed view of HR-SPD data (295 K) for $La_{2-x}Pr_xNiO_{4+\delta}$ series. Assigned space groups in this study are marked on the left near the composition (*x*). Numerous weak intensity non-indexed peaks are clear for compositions with *x* > 1.0. Main peaks are labeled with *hkl* indexing for a generic *F*-centered orthorhombic cell (*hkl* condition; all *even* or all *odd*). Characteristic positions of (212) and (032) superlattice reflections allowed in *Bmab* and $P4_2/ncm$ space groups that arise from ordered in-plane tilting of NiO_6 octahedra are marked by §. NiO impurity peaks (cubic $Fm3m$ cell with a = 4.176 Å) are marked.

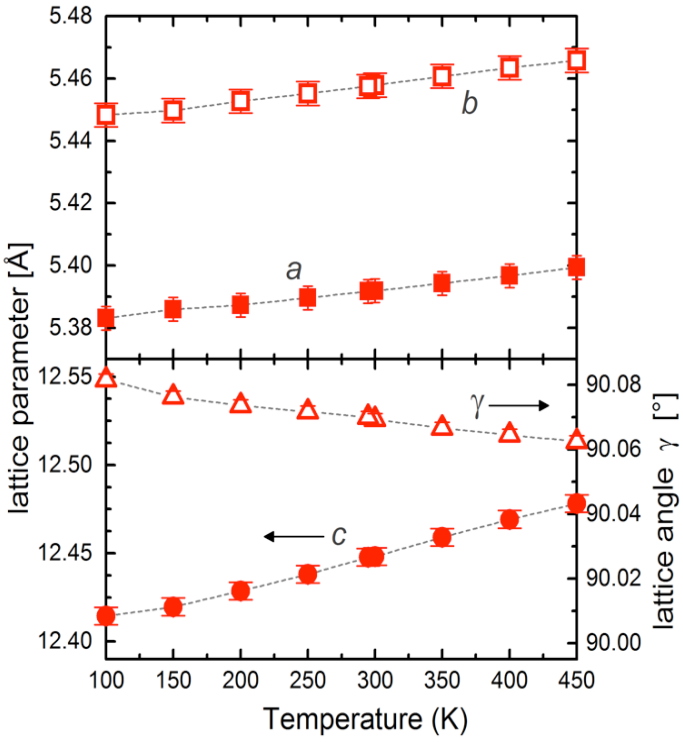

Supplemental Figure S4: Evolution of refined lattice parameters (*a, b, c*, γ) as a function of temperature for $Pr_2NiO_{4.25}$. Lattice values were obtained from refinements of *in-situ* variable temperature HR-SPD data using the *F*2/m monoclinic unit cell.

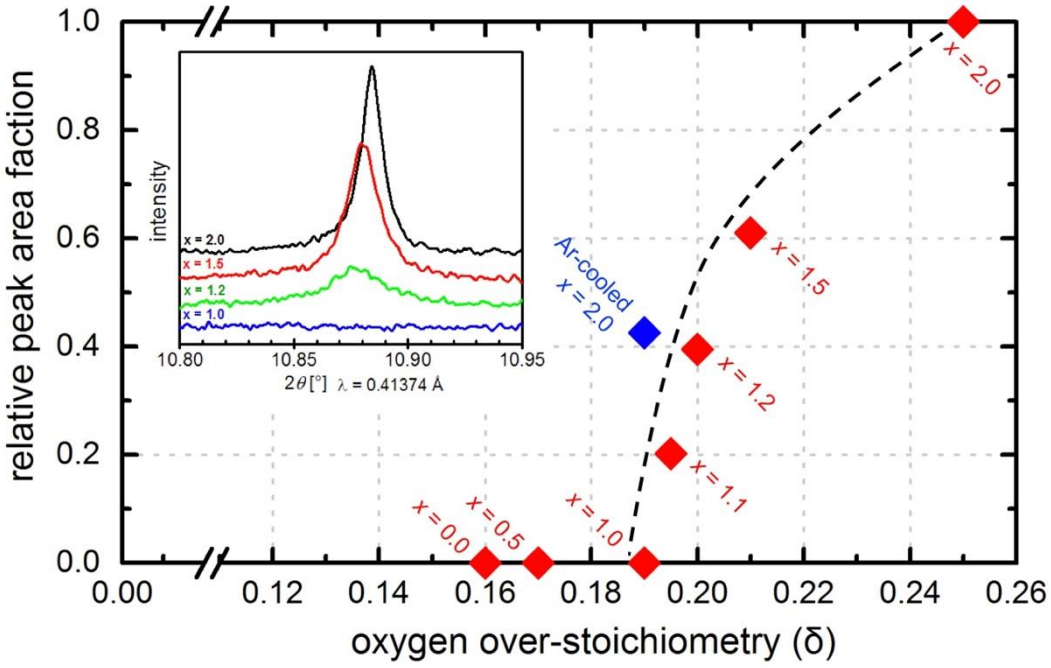

Supplemental Figure S5: Evolution of the relative integrated peak area fraction observed in HR-SPD data at room temperature as a function of oxygen over-stoichiometry (δ) for Pr-rich $La_{2-x}Pr_xNiO_{4+\delta}$ compositions. The small inset upper figure inset plots the evolution of the reference non-indexed weak intensity peak (at 2θ ≈ 10.88°) for select air-cooled compositions. The integrated peak area was defined as 1.0 for δ = 0.25, and normalized for each scan as a fraction of the integrated area for a *F*2/*m* indexed (004) peak at 2θ ≈ 7.60°. Red plotted diamonds show air-cooled samples; the blue diamond represents the Ar-cooled *x* = 2.0 sample with reduced δ. The dashed black curve is a guide for the eye. See main text Section 4.4 for details and discussion.

Supplemental Table S1: Summary of Rietveld refined structural parameters and fit statistics for compositions (*x*) in the $La_{2-x}Pr_xNiO_{4+\delta}$ system. Refined values are followed by the uncertainty in brackets. The lack of an uncertainty value indicates a fixed non-refined parameter. Other symbols described in footnotes below.

				region of 2-phase coexistence												
Composition (*x*)	0.0	0.25	0.4	0.5		0.6		0.8		1.0		1.1	1.2	1.5	2.0	2.0 (Ar cooled)
Space Group †	*Fmmm*	*F*4/*mmm*	*F*4/*mmm*	*F*2/*m*	*F*4/*mmm*	*F*2/*m*	*F*4/*mmm*	*F*2/*m*	*F*4/*mmm*	*F*2/*m*	*F*4/*mmm*	*F*2/*m*	*F*2/*m*	*F*2/*m*	*F*2/*m*	*F*2/*m*
weight fraction ▲	--	--	--	0.66	0.34	0.76	0.24	0.84	0.16	0.92	0.08	--	--	--	--	--
a (Å)	5.45985(1)	5.45992(1)	5.45700(1)	5.44209(2)	5.45492(2)	5.43737(2)	5.45279(3)	5.42874(1)	5.44904(2)	5.42111(1)	5.44482(2)	5.41771(1)	5.41440(1)	5.40572(1)	5.39172(1)	5.39757(1)
b (Å)	5.46471(1)	= *a*	= *a*	5.46796(2)	= *a*	5.46892(2)	= *a*	5.46962(1)	= *a*	5.46904(1)	= *a*	5.46865(1)	5.46809(1)	5.46422(1)	5.45749(1)	5.45416(1)
c (Å)	12.6862(2)	12.6582(1)	12.6414(1)	12.6396(3)	12.6315(2)	12.6195(2)	12.6207(1)	12.5939(1)	12.5952(1)	12.5706(2)	12.5702(1)	12.5572(2)	12.5443(1)	12.5091(1)	12.4478(1)	12.4386(2)
g (°)	90	90	90	90.003(1)	90	90.003(2)	90	90.005(2)	90	90.010(2)	90	90.011(2)	90.026(2)	90.047(2)	90.070(2)	90.062(2)
Vol. (Å^3), Z = 4	378.510(1)	377.351(1)	376.447(1)	375.888(1)	375.867(2)	375.259(1)	375.251(4)	373.994(1)	373.976(3)	372.695(1)	372.656(1)	372.036(1)	371.391(1)	369.495(1)	366.278(1)	366.181(1)
Pr/La (0, 0, *z*)	0.36064	0.36046(1)	0.36040(1)	0.36042(4)	0.36020(5)	0.36025(3)	0.36036(9)	0.36024(3)	0.35946(9)	0.36017(2)	0.3584(2)	0.35993(2)	0.35994(2)	0.35960(2)	0.35910(2)	0.35958(2)
fixed occupancy	$La_{1.0}$	$Pr_{0.125}La_{0.87}$	$Pr_{0.20}La_{0.80}$	$Pr_{0.25}La_{0.75}$		$Pr_{0.30}La_{0.70}$		$Pr_{0.40}La_{0.60}$		$Pr_{0.50}La_{0.50}$		$Pr_{0.55}La_{0.45}$	$Pr_{0.60}La_{0.40}$	$Pr_{0.75}La_{0.25}$	$Pr_{1.0}$	$Pr_{1.0}$
U_{iso} ×100 (Å^2)	0.75(1)	0.88(1)	0.91(1)	0.88(1)		0.82(1)		0.84(1)		0.85(1)		0.82*	0.91*	0.96*	0.95*	1.02(1)
Ni (0, 0, 0)																
U_{iso} ×100 (Å^2)	0.32(1)	0.46(1)	0.48(1)	0.47(2)		0.52(2)		0.41(2)		0.41(1)		0.52*	0.59*	0.54*	0.55*	0.46(1)
O(1) (0, 0, *z*)	0.1722(2)	0.1729(1)	0.1727(2)	0.1732(2)		0.1734(1)		0.1741(2)		0.1741(2)		0.1740(3)	0.1733(1)	0.1730(1)	0.1731(1)	0.1743(2)
U_{iso} ×100 (Å^2)	2.94(2)	2.9*	3.18*	4.1(2)	2.2(2)	4.78*	2.29*	3.8(1)	1.5(1)	4.65*	2.2(3)	5.00*	5.02*	5.29*	6.16*	3.96(6)
O(2) (¼, ¼, 0)																
U_{iso} ×100 (Å^2)	1.06(2)	0.86(4)	0.96(4)	1.17(5)		1.15(2)		0.93(5)		0.95(5)		0.96(6)	1.51*	1.45*	1.73*	1.51(6)
O(3) (¾, ¼, 0)																
U_{iso} ×100 (Å^2)	--	--	--	1.17(5)	--	1.15(2)	--	0.93(5)	--	0.95(5)	--	0.96(6)	1.66*	1.75*	1.76*	1.43(8)
O(4) (¼, ¼, ¼)																
U_{iso} ×100 (Å^2)	1.06(2)	0.86(4)	0.96(4)	1.17(5)		1.15(2)		0.93(5)		0.95(5)		1.5(3)	2.9(3)	2.9(3)	2.59(3)	2.6(1)
occupancy	0.08	0.08	0.08	0.06(3)		0.08(2)		0.09(2)		0.09(2)		0.10(1)	0.11(1)	0.11(1)	0.12(1)	0.08(1)
oxygen δ estimate §	0.16	0.16	0.16	0.17		0.17		0.18		0.19		0.20	0.20	0.21	0.25	0.19
δ (diffraction)	0.16	0.16	0.16	0.13(5)		0.16(3)		0.18(3)		0.18(3)		0.20(2)	0.20(2)	0.22(2)	0.24(2)	0.17(2)
δ (TGA)	0.16	--	--	0.17		--		--		0.19		--	--	0.21	0.25	0.19
refined data sets ❖	SPD	SPD	SPD	SPD		SPD+NPD		SPD		SPD		SPD	SPD+NPD	SPD+NPD	SPD+NPD	SPD
SPD R_{wp}	9.68%	11.44%	10.73%	12.91%		13.62%		13.21%		13.87%		15.61%	13.46%	12.1%	12.8%	10.6%
SPD+NPD R_{wp}	--	--	--	--		11.85%		--		--		--	10.97%	10.6%	10.4%	--
Total Reduced χ^2	4.32	6.40	7.18	11.69		16.88		11.97		13.72		8.95	13.97	12.79	10.01	6.49

Footnotes

† *F*2/*m* (full name *F*112/*m*) is a non-standard setting of *C*2/*m* (no 12); *F*4/*mmm* is a non-standard *I*4/*mmm* setting (no 139)

▲ refined phase weight fractions for 2-phase compositions

§ estimated oxygen δ values reported in Table 1; determined (primarily) from TGA data or from (secondarily) diffraction data structural refinements

* U_{iso} equivalent for refined U_{aniso} values (see supplemental information)

❖ Synchrotron Powder Diffraction (SPD), Neutron Powder Diffraction (NPD)

Supplemental Table S2: Summary of Rietveld refined anisotropic displacement parameter (ADP) values (U_{aniso}) for selected Pr-rich compositions (x) in the $La_{2-x}Pr_xNiO_{4+\delta}$ system.

Composition (x)	1.1	1.2	1.5	2.0
Space Group	*F*2/*m*	*F*2/*m*	*F*2/*m*	*F*2/*m*
refined data sets	SPD	SPD+NPD	SPD+NPD	SPD+NPD
Pr/La: U_{aniso} ×100 (Å^2)				
U11	0.69(1)	0.77(1)	0.85(1)	0.84(1)
U22	0.99(1)	1.19(1)	1.26(1)	1.34(1)
U33	0.74(1)	0.76(1)	0.75(1)	0.67(1)
U12	-0.18(4)	-0.14(1)	-0.22(1)	-0.24(1)
Ni: U_{aniso} ×100 (Å^2)				
U11	0.23(4)	0.37(2)	0.26(2)	0.22(2)
U22	0.16(4)	0.32(3)	0.30(2)	0.25(2)
U33	0.92(4)	1.07(2)	1.05(2)	1.17(3)
U12	-0.2(1)	-0.25(3)	0.18(3)	-1.10(3)
O(1): U_{aniso} ×100 (Å^2)				
U11	4.9(3)	5.30(8)	5.23(8)	5.91(8)
U22	9.9(4)	9.15(12)	10.06(12)	11.90(12)
U33	0.1(2)	0.61(5)	0.59(5)	0.69(5)
U12	6.4(4)	6.02(11)	5.30(12)	5.41(13)
O(2): U_{aniso} ×100 (Å^2)				
U11	–	0.90(11)	0.71(14)	0.82(11)
U22	–	0.31(13)	0.27(14)	0.33(11)
U33	–	3.63(30)	3.36(31)	4.14(29)
U12	–	-0.40(8)	-0.27(8)	-0.25(7)
O(3): U_{aniso} ×100 (Å^2)				
U11	–	0.39(10)	0.34(13)	0.26(10)
U22	–	0.95(12)	0.57(15)	0.53(11)
U33	–	3.64(33)	4.34(35)	4.38(30)
U12	–	0.18(7)	0.21(8)	0.21(6)

Supplemental Table S3: Summary of selected bond distances determined from Rietveld refined structural models for compositions (x) in the $La_{2-x}Pr_xNiO_{4+\delta}$ system.

				region of 2-phase coexistence												
Composition (x)	0.0	0.25	0.4	0.5		0.6		0.8		1.0		1.1	1.2	1.5	2.0	2.0 (Ar cooled)
Space Group	*Fmmm*	*F*4/*mmm*	*F*4/*mmm*	*F*2/*m*	*F*4/*mmm*	*F*2/*m*	*F*4/*mmm*	*F*2/*m*	*F*4/*mmm*	*F*2/*m*	*F*4/*mmm*	*F*2/*m*	*F*2/*m*	*F*2/*m*	*F*2/*m*	*F*2/*m*
refined data sets	SPD	SPD	SPD	SPD		SPD+NPD		SPD		SPD		SPD	SPD+NPD	SPD+NPD	SPD+NPD	SPD
Ni-O(1) (x2)	2.198(2)	2.188(2)	2.183(2)	2.188(3)	2.188(3)	2.188(2)	2.1878(2)	2.193(3)	2.193(3)	2.1886(2)	2.189(2)	2.185(3)	2.173(1)	2.164(1)	2.155(1)	2.168(3)
Ni-O(2) (x2, x4) †	1.9312(2)	1.9304(2)	1.9293(2)	1.9286(1)	1.9286(1)	1.9278(1)	1.9282(1)	1.9265(1)	1.9265(1)	1.9249(1)	1.9250(2)	1.9243(3)	1.9233(1)	1.9208(1)	1.9167(1)	1.9173(1)
Ni-O(3) (x2)	–	–	--	–	1.9287(1)	–	1.9278(1)	–	1.9268(1)	–	1.9253(2)	1.9246(3)	1.9242(1)	1.9224(1)	1.9191(1)	1.9194(1)
Pr/La-O(1) (x1)	2.378(2)	2.374(2)	2.373(2)	2.362(3)	2.365(3)	2.359(2)	2.359(2)	2.334(3)	2.344(3)	2.316(2)	2.3388(3)	2.335(3)	2.3417(2)	2.3338(2)	2.315(2)	2.305(3)
Pr/La-O(1) (x2, x4) †	2.7635(3)	2.7624(3)	2.7604(3)	2.7599(4)	2.7668(4)	2.7592(3)	2.7672(2)	2.7572(4)	2.7689(4)	2.7527(3)	2.7683(2)	2.7673(5)	2.7656(2)	2.7624(2)	2.7581(2)	2.7594(4)
Pr/La-O(1) (x2)	–	–	--	–	2.7540(4)	–	2.7516(2)	–	2.7487(4)	–	2.7445(1)	2.7422(5)	2.7390(2)	2.7335(2)	2.7255(2)	2.7315(4)
Pr/La-O(2) (x2, x4) †	2.6182(2)	2.6166(2)	2.6147(1)	2.6149(4)	2.6131(3)	2.6129(8)	2.6126(3)	2.6163(8)	2.6097(2)	2.6220(14)	2.6070(2)	2.6070(2)	2.6050(2)	2.6039(2)	2.5998(2)	2.5936(1)
Pr/La-O(3) (x2)	–	–	--	–	2.6132(3)	–	2.6128(3)	–	2.6096(2)	–	2.6068(2)	2.6073(2)	2.6057(2)	2.6027(2)	2.5981(2)	2.5951(1)
Pr/La-O(4) (x2)	2.3874(2)	2.3835(1)	2.3812(2)	2.3785(4)	2.3801(3)	2.3776(7)	2.3776(2)	2.3690(7)	2.3748(2)	2.3582(12)	2.3714(2)	2.3682(2)	2.3667(2)	2.3599(2)	2.3491(2)	2.3525(1)
Pr/La-O(4) (x2)	2.3874(2)	2.3835(1)	2.3812(2)	2.3785(4)	2.3802(3)	2.3776(7)	2.3779(2)	2.3690(7)	2.3749(2)	2.3582(12)	2.3716(2)	2.3685(2)	2.3674(2)	2.3612(2)	2.3510(2)	2.3542(1)

† Bond multiplicity is x2 for *F*2/*m*, but x4 for *F*4/*mmm* and *Fmmm* models, where O(2) and O(3) sites are equivalent